Journal of Non-Newtonian Fluid Mechanics 201 (2013) 10–16

Contents lists available at SciVerse ScienceDirect

Journal of Non-Newtonian Fluid Mechanics

journal homepage: http://www.elsevier.com/locate/jnnfm

Viscoelastic secondary flows in serpentine channels

R.J. Poole [a,*], A. Lindner [b], M.A. Alves [c]

[a] School of Eng., University of Liverpool, Brownlow Hill, Liverpool L69 3GH, UK
[b] PMMH, ESPCI, UPMC, Univ., Denis-Diderot CNRS UMR 7636 10, rue Vauquelin, F-75231 Paris Cedex 05, France
[c] Departamento de Engenharia Química, Faculdade de Engenharia da Universidade do Porto, Rua Dr. Roberto Frias, 4200-465 Porto, Portugal

ARTICLE INFO

Article history:
Received 16 April 2013
Received in revised form 4 July 2013
Accepted 4 July 2013
Available online 15 July 2013

Keywords:
Finite volume method
Oldroyd-B model
UCM model
Secondary flow
Serpentine channel

ABSTRACT

We report the results of a detailed numerical investigation of inertialess viscoelastic fluid flow through three-dimensional serpentine (or wavy) channels of varying radius of curvature and aspect ratio using the Oldroyd-B model. The results reveal the existence of a secondary flow which is absent for the equivalent Newtonian fluid flow. The secondary flow arises due to the curvature of the geometry and the streamwise first normal–stress differences generated in the flowing fluid and can be thought of as the viscoelastic equivalent of Dean vortices. The effects of radius of curvature, aspect ratio and solvent-to-total viscosity ratio on the strength of the secondary flow are investigated. The secondary flow strength is shown to be a function of a modified Deborah number over a wide parameter range.

1. Introduction

It is well known that flows within pipes and ducts can give rise to secondary flows. In addition to the base primary flow in the streamwise direction, a secondary flow, albeit usually much weaker, can develop in the cross-stream direction. In the case of Newtonian fluids, so-called Dean vortices [1,2] appear in curved ducts or bends and are a consequence of flow inertia. Dean flow gives rise to a pair of vortices in the cross-section carrying flow from the inside to the outside of the bend across the centre and back around the edges. (NB: Malheiro et al. [3] have recently studied the effect of elasticity on such vortices). For Newtonian fluids in the absence of inertia, or in the absence of curvature, i.e. in straight pipes and ducts of uniform cross-section, there is no physical driving mechanism for a secondary flow and the laminar flow remains unidirectional. Interestingly, Lauga et al. [4] show that a secondary flow must develop if a channel has *both* varying cross-sectional area and non-constant curvature even in the creeping-flow limit. Note that turbulent flow can give rise to a secondary flow even in the case of straight ducts as long as the geometry is non-axisymmetric [5,6] i.e. not a circular pipe or a concentric annulus.

For viscoelastic fluid flows, in contrast, secondary flows can develop in the absence of inertia and curvature. Weak secondary flows are observed even for straight ducts of uniform cross-section as long as the geometry is non-axisymmetric. Such elastically-induced secondary flows are driven by imbalances in the second-normal stress difference and have been studied in detail by a number of authors [7–12]. Interestingly, Speziale [13] highlighted the relationship between this type of secondary flow and that driven by turbulence as discussed above. As the magnitude of the second-normal–stress difference is usually very small for most dilute polymer solutions, being estimated to be at most 20% of the first normal–stress difference for concentrated solutions and melts [14], these secondary flows tend to be extremely weak being of the order of 1% or less of the primary streamwise velocity [9]. As a consequence, numerical simulations of viscoelastic constitutive equations which predict a zero second normal–stress difference, such as the upper-convected Maxwell and Oldroyd-B models [15], the simplified Phan–Thien–Tanner (PTT) model [16] and FENE-type models [17,18], all predict unidirectional flow in such straight ducts, at least prior to the appearance of purely-elastic instabilities beyond a critical Weissenberg number [19].

The combined case of duct curvature and fluid elasticity in the inertialess limit, which has been significantly less studied, can also give rise to secondary flows. These secondary flows can occur in both axisymmetric as well as non-axisymmetric geometries and can be observed even for fluids which exhibit a zero second normal–stress difference in steady simple shear flow. This has been elegantly shown by Fan et al. [20] who investigated flow in curved pipes. To the best of our knowledge, for flows in non-axisymmetric

* Corresponding author. Tel.: +44 151 794 4806; fax: +44 151 794 4848.
E-mail addresses: robpoole@liv.ac.uk (R.J. Poole), anke.lindner@espci.fr (A. Lindner), mmalves@fe.up.pt (M.A. Alves).

0377-0257
http://dx.doi.org/10.1016/j.jnnfm.2013.07.001

geometries the only paper which investigates inertialess secondary flows is the recent work by Norouzi et al. [21]. They use the second-order fluid model [22] to investigate curved ducts with square cross-sections both with and without inertia. By varying the parameters in the second-order fluid model to control the ratio of first to second normal–stress differences, Norouzi et al. were able to show that the strength and direction of the secondary flow could be varied. When the first normal–stress difference was dominant the direction of the viscoelastic secondary flow was found to be in the same sense as that observed by Fan et al. [20], i.e. in the same sense as inertial Dean flow, but when the first normal–stress difference was zero and only second normal–stresses occurred the secondary flow changed direction. The second-order fluid used by Norouzi et al. is appropriate in the limit of vanishingly small elasticity, and therefore to small Deborah numbers, and is thus useful to investigate the qualitative behaviour of polymer flow phenomena such as the direction of secondary flows. The quantitative prediction of the strength of the secondary flow beyond the asymptotic limit of vanishingly elasticity will be influenced by the choice of constitutive equation and the effects of more realistic constitutive equations on the strength of this elastically-driven secondary flow has not been investigated. In the current paper we report the results of a detailed numerical investigation of inertialess viscoelastic fluid flow through three-dimensional serpentine (or wavy) channels [23,24] of varying radius and aspect ratios using the Oldroyd-B model to fully explore this secondary flow regime. Such serpentine channels are composed of a series of circular half loops of alternating curvature and represent prototype geometries for investigating curvature effects experimentally [23,24].

2. Viscoelastic constitutive equation and numerical method

The three-dimensional numerical simulations assume isothermal flow of an incompressible viscoelastic fluid described by the Oldroyd-B model [15] in a channel of rectangular cross section. The equations that need to be solved are those of mass conservation,

$$\nabla \cdot \mathbf{u} = 0, \tag{1}$$

and momentum

$$\mathbf{0} = -\nabla p + \eta_s \nabla^2 \mathbf{u} + \nabla \cdot \boldsymbol{\tau}, \tag{2}$$

assuming creeping-flow conditions (i.e. the inertial terms are exactly zero), where $\mathbf{u}$ is the velocity vector with Cartesian components (u_x, u_y, u_z), p is the pressure and η_s is the solvent viscosity. For the Oldroyd-B model the evolution equation for the polymeric extra-stress tensor, $\boldsymbol{\tau}$, is

$$\boldsymbol{\tau} + \lambda\left(\frac{\partial \boldsymbol{\tau}}{\partial t} + \mathbf{u}\cdot\nabla\boldsymbol{\tau}\right) = \eta_p(\nabla\mathbf{u} + \nabla\mathbf{u}^T) + \lambda(\boldsymbol{\tau}\cdot\nabla\mathbf{u} + \nabla\mathbf{u}^T\cdot\boldsymbol{\tau}), \tag{3}$$

where λ and η_p are the relaxation time and polymeric contribution to the viscosity of the fluid respectively, both of which are constant in this model. For a large number of simulations shown here we set the solvent viscosity contribution to zero and, in this case, the upper-convected Maxwell (UCM) model is recovered.

Although the Oldroyd-B model exhibits an unbounded steady-state extensional viscosity above a critical strain rate ($1/2\lambda$), in shear-dominated serpentine channel geometries such model deficiencies are unimportant and it is arguably the simplest differential constitutive equation which can capture many aspects of highly-elastic flows [25,26]. Many more complex models (e.g. the FENE-P, Giesekus and Phan–Thien–Tanner models – see e.g. Bird et al. [22]), simplify to the Oldroyd-B model in certain parameter limits and thus its generality makes it an ideal candidate for fundamental studies of viscoelastic fluid flow behaviour. The governing equations are solved using a time-marching implicit finite-volume numerical method, based on the logarithm transformation of the conformation tensor [27]. Additional details about the numerical method can be found in Afonso et al. [28,29] and in other previous studies (e.g. [30,31]). For low Wi the numerical solution converges to a steady solution, which was assumed to occur when the L_2 norm of the residuals of all variables reached a tolerance of 10^{-6}. Beyond a critical Weissenberg number a time-dependent purely-elastic instability occurs [24]. The results in the current paper are restricted to Weissenberg numbers below the occurrence of this purely-elastic instability: thus the flow remains steady.

3. Flow geometry, dimensionless numbers and computational meshes

The serpentine channels used in this work consist of a series of half-loops of width W, height H and inner radius R as shown schematically in Fig. 1. Although the geometries are fully three-dimensional we impose a symmetry boundary condition on the xy-centreplane to reduce the computational burden. Limited simulations on the complete domain confirmed that, for the steady results shown here, the imposition of symmetry has no effect on the results. In all the results which follow the symmetry plane is highlighted by a dashed boundary (see Fig. 1c for example). The inner and outer walls are also indicated. A series of geometries were created such that the effects of radius (R/W) and aspect ratio ($a = W/H$) could be investigated in the range $1 \leqslant R/W \leqslant 7$ and $0.5 \leqslant W/H \leqslant 4$.

For all results shown in this work the Reynolds number is identically zero. The Weissenberg number is defined as $Wi = \lambda U/W$, where λ is the relaxation time of the fluid and U/W represents a characteristic shear rate based on the channel width W and the bulk velocity U in the channel. A Deborah number can be defined as $De = \lambda U/R$ based on the ratio of the relaxation time of the fluid and a characteristic residence time in each half loop ($\sim R/U$).

The number of full(half) loops in each geometry was fixed at two(four): tests with more loops gave identical results. The majority of data pertaining to the secondary flow will be presented at the bend in the first half loop (location A1 in Fig. 1b). For the current results, where the Deborah number remains always less than one, memory effects remain small and secondary flow data at subsequent loops (e.g. A3 or B1) are essentially identical to the first loop (in the least favourable case for example when $R/W = 1$, $W/H = 1$ and $Wi = 0.6$ the secondary flow strength, as measured by the maximum spanwise velocity, differs by just 0.7% between locations A1, A3, B1 and B3).

For all of the serpentine channels the computational domain was mapped using three orthogonal blocks, one straight inlet section of length 10 W, one block comprising four half loops of varying curvature and a final straight exit section also 10 W in length. The main characteristics of the meshes are provided in Table 1. The information in Table 1 includes the total number of cells in the meshes (NC) together with the number of control volumes in each direction (NX, NY and NZ) and the total number of degrees of freedom (DOF) of the computed variables. The cell sizes are uniform in the y- and z-directions and in the x-direction in the second block. In the inlet(exit) channels the cell spacing in the x-direction decreases as the cells move towards(away) from the block containing the half-loops. It is important to note that the x, y, z coordinate system is fixed in space but that we will refer always to the velocity component in the streamwise direction as u, in the wall normal or transverse direction as v and the velocity in the spanwise direction (z) as w. As a consequence the streamwise velocity component u for example is only aligned with the x-direction in the straight inlet and outlet channels (and at locations A2, A4/B0, B2). Thus

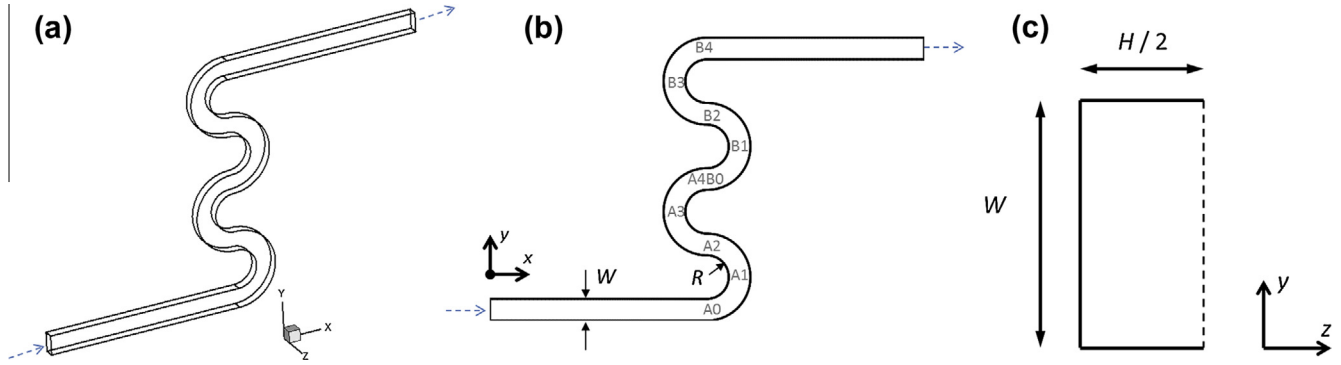

Fig. 1. Schematic of the serpentine channel (a) isometric view; (b) bird's eye view including location nomenclature; and (c) cross-sectional view. Blue arrows indicate flow direction. (For interpretation of the references to colour in this figure legend, the reader is referred to the web version of this article.)

Table 1
Main characteristics of computational meshes.

W/*H*	*R*/*W*	NX	NY	NZ	NC	DOF
1	1	600	25	25	375,000	3.75×10^6
	3	1000	25	25	625,000	6.25×10^6
	5	1600	25	25	1,000,000	10.0×10^6
	7	1800	25	25	1,125,000	11.25×10^6
1/2	1	600	25	50	750,000	7.5×10^6
2	1	600	25	25	375,000	3.75×10^6
4	1	600	25	13	195,000	1.95×10^6

at location A0 the wall normal (or transverse) velocity is the velocity component in the *y*-direction but at A1, i.e. after the flow turns 90°, it is the component in the *x*-direction. By contrast the velocity in the *z*-direction (the "neutral" or "spanwise" direction) is always *w* but we consider *w* to be positive pointing in the direction from the side wall (top/bottom) towards the *xy*-symmetry plane (thus pointing in opposite directions on both sides of the *xy*-symmetry plane).

4. Discussion

4.1. Qualitative description of secondary flow

In Fig. 2 we plot contours of the three velocity components in a *xz*-plane at the outer bend in the first half loop, i.e. location A1 identified in Fig. 1b, for both the Newtonian fluid and a viscoelastic fluid (UCM model, $Wi = 0.2$). The data is shown for $R/W = 1$ and $W/H = 1$. We remark that the *w* velocity is considered positive in the direction of the *xy*-symmetry plane, as illustrated by the arrow in Fig. 2c). As expected in the total absence of inertia for the Newtonian fluid the only non-zero component is the streamwise velocity component. The transverse and spanwise velocities are zero. For the viscoelastic fluid, although the streamwise velocity contours are qualitatively similar, a weak secondary flow is clearly apparent: the positive transverse velocity at the centreline indicates flow moving from the inner wall towards the outer wall which, in turn, is fed from fluid at the outer wall transported along the side wall. At this Weissenberg number the strength of the secondary flow components are strongest in the transverse direction (i.e. $v > w$) and are at maximum 3–4% of the bulk streamwise velocity.

4.2. Projected streamlines

To further highlight the nature of the secondary flows, in Fig. 3 we show projected streamlines again in the *xz*-plane at the first outer bend (location A1) for various aspect ratios at a single radius ratio ($R/W = 1$). We remark that although each projected streamline plotted seems to be closed, indeed the starting point and the end point do not coincide exactly. As could be inferred from the secondary flow velocity contours in Fig. 2, the secondary flow gives rise, at least for $a \geqslant 1$, to a pair of vortices – only one of which is

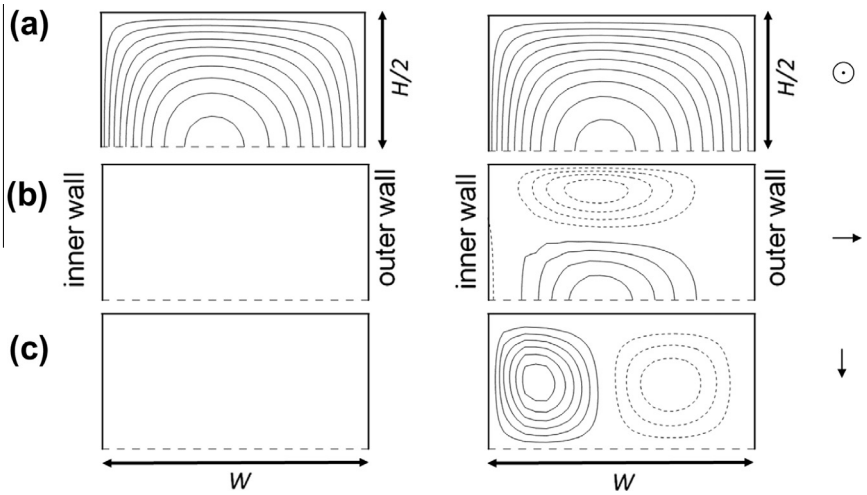

Fig. 2. Velocity contours for Newtonian fluid (LHS) and UCM fluid at $Wi = 0.2$ (RHS) in a *YZ* plane at location A1 for $R/W = 1$, $a = W/H = 1$; (a) streamwise velocity contours u/U (0.2–2.0 in steps of 0.2), (b) transverse contours v/U (−0.04 to +0.04 in steps of 0.01 for $Wi = 0.2$ only, Newtonian velocities $< 2 \times 10^{-5}$), (c) spanwise contours w/U (−0.015 to 0.030 steps of 0.005 for $Wi = 0.2$ only, Newtonian velocities $< 10^{-5}$). Negative contours indicated by short dashed lines and the *xy*-centreplane by long dashed lines.

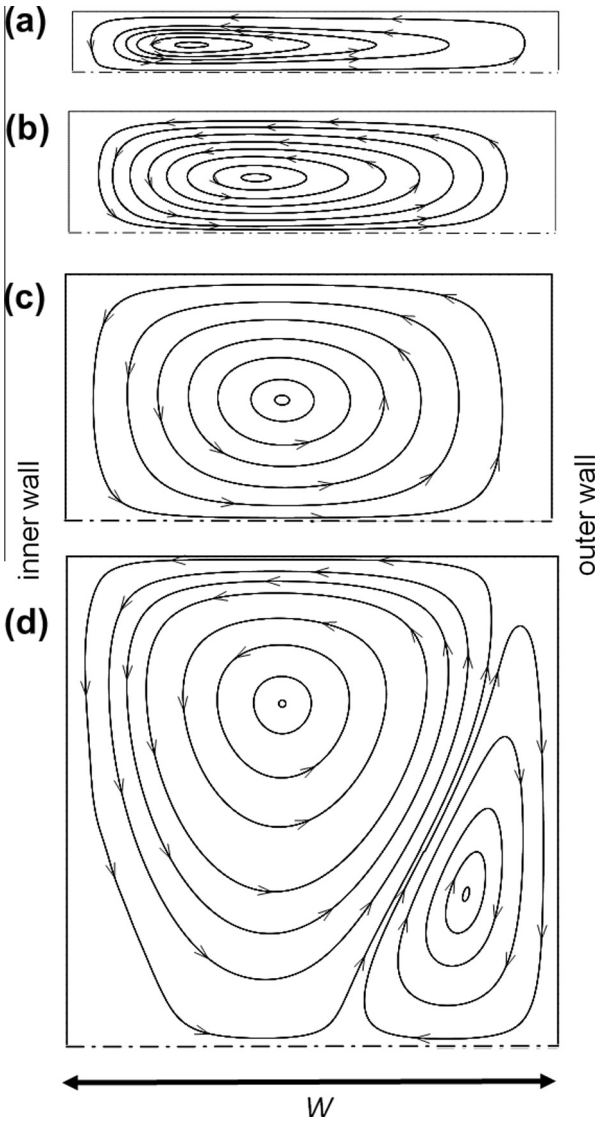

Fig. 3. Effect of aspect ratio (a) on projected streamlines in a xz plane at location A1 shown for $R/W = 1$ UCM model, at $Wi = 0.1$; (a) $a = 4$, (b) $a = 2$ (c) $a = 1$ and (d) $a = 0.5$.

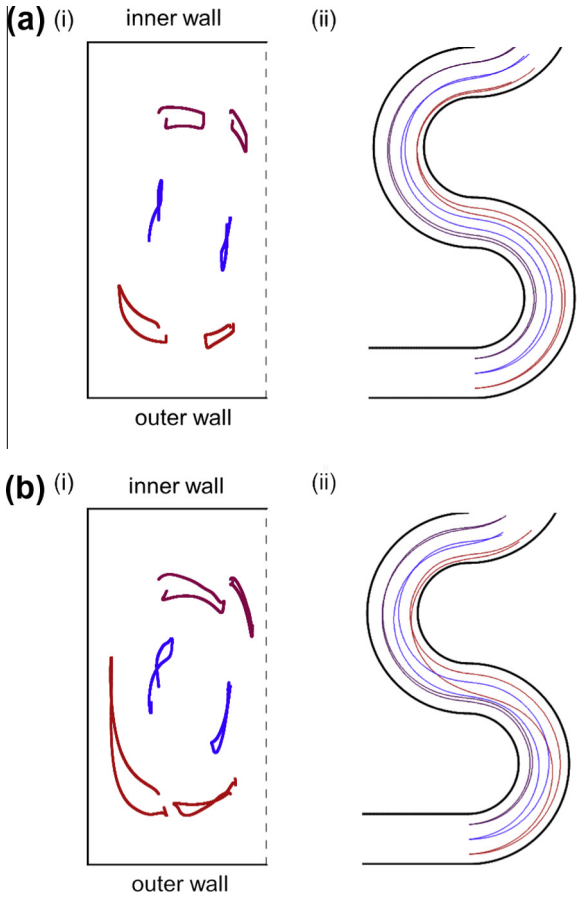

Fig. 4. (i) Projection of 3D trajectories taken by streamtraces in first loop onto a 2D plane normal to streamwise direction; (ii) Bird's eye view of 3D trajectories of streamtraces. Released from $x = 0$ plane, location A0, and $(z/H, y/W)$ locations of (0.2,0.2), (0.4,0.2), (0.2,0.5), (0.4,0.5), (0.2,0.8) and (0.4,0.8); (a) $R/W = 1$, $a = 1$, $Wi = 0.3$; (b) $R/W = 1$, $a = 1$, $Wi = 0.6$.

simulated and shown here due to the symmetry boundary condition – carrying flow from the inside wall to the outside wall along the centreline and back to the inner wall along the sidewall.

At lower aspect ratio, i.e. in a deeper channel, additional vortices appear. The strength of the additional vortex close to the outer wall is about 100 times smaller than the primary vortex and is thus extremely weak.

In order to elucidate the full effect of the secondary flow, Fig. 4 shows 2D projections of 3D trajectories for six fluid elements released at the entrance to the first loop (location A0 in Fig. 1b). The pathlines are determined through numerical integration of the flow field: $d\mathbf{x}/dt = \mathbf{u}$. Fig. 4i plots the projection of these 3D trajectories onto a 2D plane normal to the streamwise direction so that information regarding the trajectory can be more easily visualised and Fig. 4ii highlights 2D projections viewed "from above" as is usually done experimentally using streak photography in microfluidics (see e.g. [23,24]). The trajectories are colour-coded with respect to their y-locations; red being trajectories released initially close to the outer wall, blue on the centreline and purple close to the inner wall. The effect of increasing elasticity is highlighted by showing data for both $Wi = 0.3$ and $Wi = 0.6$. As the secondary flow strength increases with decreasing R (discussed in Section 4.4) and increasing Wi, the latter data set represents the strongest secondary flow of all our results. Equivalent data for the Newtonian fluid, not shown, shows small vertical lines in the 2D plane-normal projections where the fluid moves towards the inner wall as it goes into the bend and then back to towards the outer wall as it comes out of the bend due to the shape of the geometry and the resulting bending of the streamlines. Within some small numerical uncertainty, much smaller than the cell size, the Newtonian pathline returns to its initial location at the end of the half-loop due to the linearity of inertialess Stokes' flow. For the viscoelastic fluid flows the non-linearity introduced by elasticity is apparent as the start and end points of the trajectories are significantly different. At $Wi = 0.3$ the secondary flow causes a fluid particle to move lateral and vertical distances on the order of 0.2 W and at the higher Weissenberg number this effect is accentuated. For example the particle initially released close to the outer and side walls (0.2,0.2) – shown in red – initially moves north west towards the inner and side walls, crosses the semi-circular centreline, before moving vertically back towards the outer wall before being swept back towards the symmetry plane. At $Wi = 0.6$ the secondary flow is strong enough such that the pathlines from different 3D trajectories, shown in Fig. 4ii as the projection from above, are appearing to cross (we note they are in different z-planes at the "crossing"). Of course for steady flow they cannot cross, otherwise the crossing point would have at the same time two different

velocities, each one pointing in the direction of each trajectory at that point.

As already discussed, the residence time of a fluid particle in each half loop is sufficiently long such that the fluid, even at the highest Weissenberg numbers analysed, essentially has time to fully relax prior to entering the subsequent loop. As a consequence, trajectories released in the second loop, i.e. from location B0 rather than A0, are identical. In Fig. 5 we make use of this fact to construct 2D projections of 3D trajectories in arbitrarily long serpentine channels. To do so we take the end (y,z) location (i.e. in A4) from the first trajectory and feed this value into a new (y,z) start point for a subsequent trajectory at location A0. In this manner we can follow trajectories for arbitrarily long times. Fig. 5a shows data for the trajectory initially released from (0.2,0.2) and followed for 60 half loops. At the end of 60 half loops the trajectory is, entirely coincidentally, almost back to its starting point (to a location of 0.20, 0.19 which is well within one cell of the trajectory origin). In Fig. 5b we show the trajectory of a near-neighbour point over the same number of half loops. (A "near-neighbour" point was selected by moving one cell away in the y-direction). Although the trajectory of the near neighbour appears qualitatively similar it is still at a considerable distance from its starting point after 60 half loops.

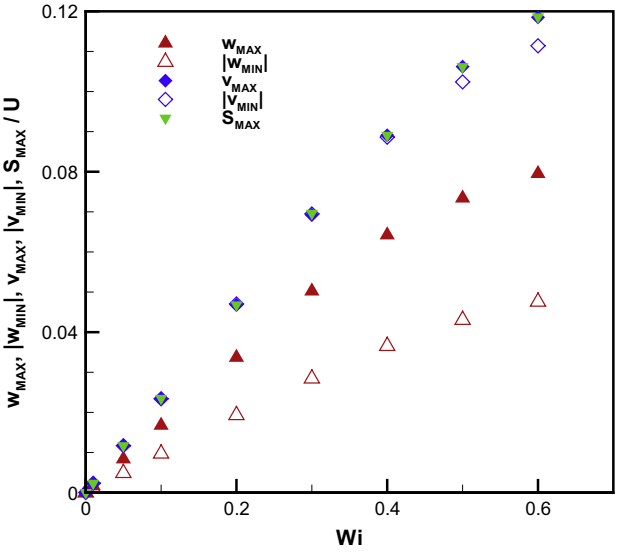

Fig. 6. Variation of secondary flow strength components at location A1 for $R/W = 1$, $a = 1$.

4.3. Strength of secondary flow

To quantify the strength of the secondary flow we can choose either the maximum positive or minimum negative velocity in either the spanwise (w) or transverse (v) directions or we can use, as others have done [20,21], the absolute value of the maximum secondary flow strength $S_{MAX} = (\sqrt{w^2 + v^2})_{MAX}$. In Fig. 6 we plot the variations of these secondary flow components at location A1 with Weissenberg number for square channels ($a = 1$) at $R/W = 1$ using the UCM model. Fig. 6 highlights that the transverse components are larger than the spanwise and that the absolute value of the secondary flow strength is dominated by the transverse component (i.e. $S_{MAX} \approx v_{MAX}$). Although the maximum positive and negative transverse velocities are similar in magnitude for lower Wi, the positive spanwise velocities (towards symmetry plane) are stronger than the negative spanwise velocities away from the symmetry centreplane. In addition each of the components scales monotonically with increasing elasticity. Although the transverse velocities are larger than the spanwise, in what follows we will use the maximum spanwise velocity at location A1 to quantify the secondary flow strength. Our rationale for this choice is twofold. Firstly, for the Newtonian simulations – where there is no secondary flow – the curvature of the geometry causes the transverse velocity to be non-zero within the geometry except at location A1 (or A3, B1, B3): thus small extrapolation errors may affect the accuracy of this quantity for small values of the secondary flow. In contrast, the spanwise velocity component is negligible near section A1 for the Newtonian fluid due to constant curvature and constant channel width [4] and therefore provides an unambiguous measure of secondary flow strength regardless of radius or aspect ratio. Secondly S_{MAX} provides no information beyond v_{MAX}.

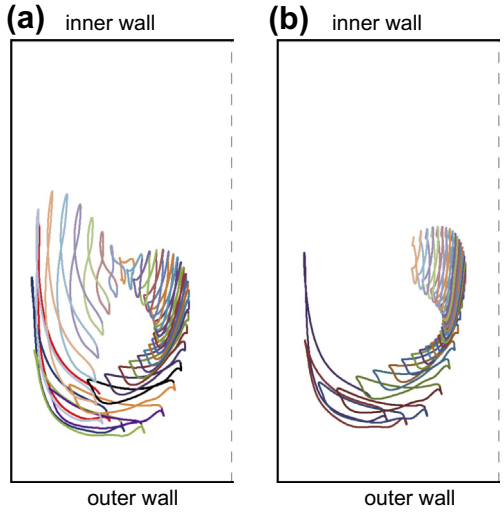

Fig. 5. Projection of 3D trajectories taken by streamtraces in series of 60 half-loops onto a 2D plane normal to streamwise direction. $R/W = 1$, $a = 1$, $Wi = 0.6$. Released from $x = 0$ plane, location A0, and $(z/H, y/W)$ locations of (a) (0.2,0.2); (b) (0.2,0.16).

The effect or curvature is shown in Fig. 7 where data for square channels are shown both in terms of Weissenberg number (Fig. 7a) and a Deborah number based on the residence time in each half loop i.e. $De = \lambda U/R$ (Fig. 7b). At constant Weissenberg number the effect of reducing the radius of curvature of the geometry increases the secondary flow strength. (Of course in the limit of infinite radius of curvature, a straight channel, the secondary flow must vanish as this model has a vanishing second-normal stress difference). When plotted in terms of Deborah number the curvature effect on the secondary flow strength becomes encapsulated in the Deborah number and the data for different geometries collapses onto a single curve. The secondary flow strength is seen to scale linearly with Deborah number over the low-moderate De range. As a time-dependent purely-elastic instability occurs just beyond the De values shown here [24] this linear scaling thus approximately holds for the entire region over which the flow remains steady.

Fig. 8 illustrates the effect of the solvent viscosity ratio, $\beta = \eta_s/(\eta_s + \eta_p)$, on the secondary flow strength for the UCM model ($\beta = 0$) and for the Oldroyd-B model considering two different solvent viscosity ratios ($\beta = 0.5$ and 0.9). To correctly incorporate solvent viscosity effects we make use of a modified[1] Deborah

[1] This definition is not really *modified* in a sense and perhaps "consistent" Deborah number is more apt as, in this manner, elastic effects are estimated as being proportional to the first normal–stress difference scaled by twice the shear stress. Instead of using solely the relaxation time to estimate a characteristic fluid time we are using the difference between the relaxation and retardation times of the Oldroyd-B model.

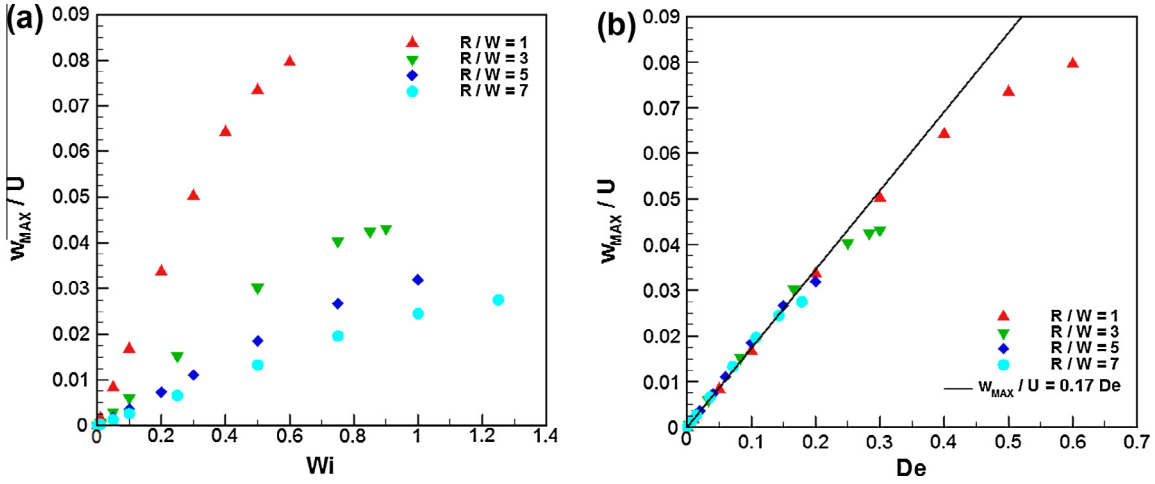

Fig. 7. Effect of curvature on maximum spanwise secondary flow velocity at location A1 for square channels ($a = 1$) and UCM model as a function of (a) Weissenberg number and (b) Deborah number (data taken from [24]).

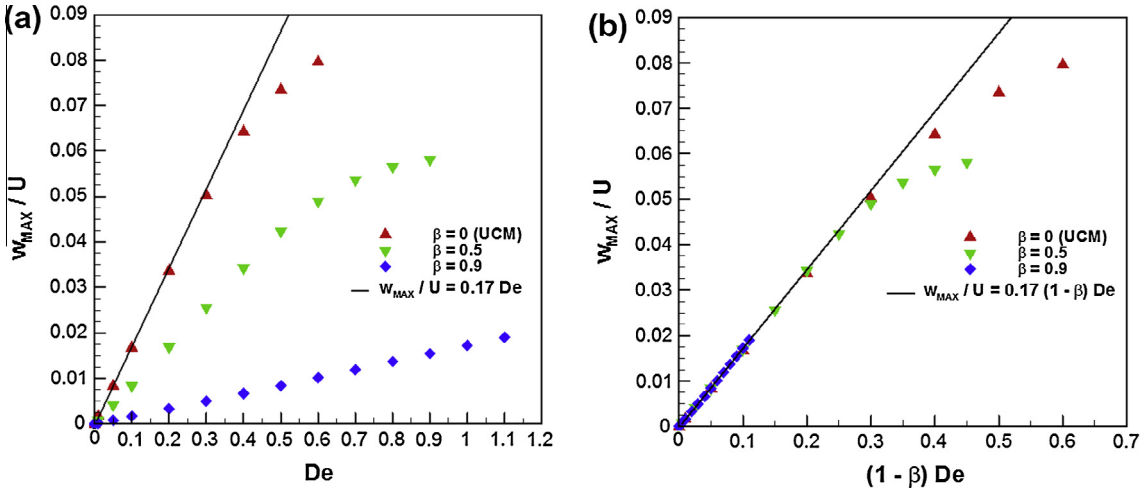

Fig. 8. Effect of solvent viscosity ratio on maximum spanwise secondary flow velocity at location A1 for a square channel ($a = 1$) and $R/W = 1$ as a function of (a) Deborah number and (b) modified Deborah number.

number equal to $(1 - \beta)\,De$ and then linear collapse of the secondary flow strength is again observed. Finally, in Fig. 9, we plot the effect of channel aspect ratio on the secondary flow strength. For $a \geqslant 1$, the strength of the secondary flow is found to be independent of the aspect ratio. For small aspect ratios, i.e. the deeper channel as shown in Fig. 3d, where the secondary flow is no longer characterised by a single pair of vortices, this simple scaling no longer holds.

5. Conclusions

The results of a systematic numerical investigation of inertialess viscoelastic fluid flow through three-dimensional serpentine (or wavy) channels of varying radius and aspect ratios using the Oldroyd-B/UCM model have revealed the existence of a secondary flow which is absent for the equivalent Newtonian fluid flow. The secondary flow arises due to the curvature of the geometry and the streamwise first normal–stress differences generated in the flowing fluid and can be thought of as the viscoelastic equivalent of Dean vortices.

The effects of radius of curvature ratio, aspect ratio and solvent-to-total viscosity ratio on the strength of the secondary flow are

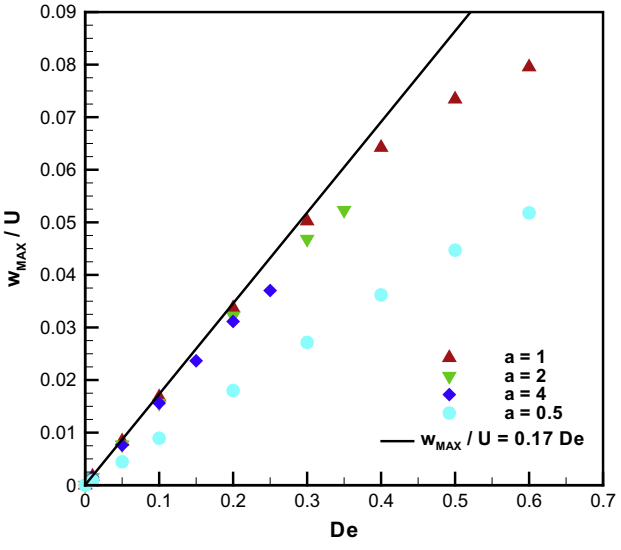

Fig. 9. Effect of aspect ratio on maximum spanwise secondary flow velocity at location A1 for $R/W = 1$ and UCM model as a function of Deborah number.

investigated and shown to be self-similar over a wide parameter range using a modified Deborah number.

Acknowledgements

Some of this work was undertaken whilst RJP was a visiting "Chaire Michelin" at the ESPCI Paris Tech in June 2012/2013 and this support is hereby gratefully acknowledged. MAA acknowledges funding from the European Research Council (ERC), under the European Commission "Ideas" Specific Programme of the Seventh Framework Programme (Grant Agreement N° 307499). We would like to thank Prof. Mike Graham (University of Wisconsin – Madison) for highlighting the paper by Lauga et al. We also thank Dr. Simon Haward (Universidade do Porto) for useful comments on a draft manuscript.

References

[1] W.R. Dean, Note on the motion of fluid in a curved pipe, Philos. Magn. 20 (1927) 208–223.
[2] W.R. Dean, The streamline motion of fluid in a curved pipe, Philos. Magn. 5 (7) (1928) 673–695.
[3] J.M. Malheiro, P.J. Oliveira, F.T. Pinho, Parametric study on the three-dimensional distribution of velocity of a FENE-CR fluid flow through a curved channel, J. Non-Newt. Fluid Mech., In press, 2013.
[4] E. Lauga, A.D. Stroock, H.A. Stone, Three-dimensional flows in slowly varying planar geometries, Phys. Fluids 16 (2004) 3051–3062.
[5] A. Melling, J.H. Whitelaw, Turbulent flow in a rectangular duct, J. Fluid Mech. 78 (1976) 289–315.
[6] M.P. Escudier, S. Smith, Fully developed turbulent flow of non-Newtonian liquids through a square duct, Proc. Roy. Soc. London A 457 (2001) 911–936.
[7] A.E. Green, R.S. Rivlin, Steady flow of non-Newtonian fluids through tubes, Q. Appl. Math. 14 (1956) 299–308.
[8] P. Townsend, K. Walters, W.M. Waterhouse, Secondary flows in pipes of square cross-section and measurements of the second normal stress difference, J. Non-Newt. Fluid Mech. 1 (1976) 107–123.
[9] B. Gervang, P.S. Larsen, Secondary flows in straight ducts of rectangular cross section, J. Non-Newt. Fluid Mech. 39 (1991) 217–237.
[10] B. Debbaut, T. Avalosse, J. Dooley, K. Hughes, On the development of secondary motions in straight channels induced by the second normal stress difference: experiments and simulations, J. Non-Newt. Fluid Mech. 69 (1997) 255–271.
[11] S.C. Xue, N. Phan-Thien, R.I. Tanner, Numerical study of secondary flows of viscoelastic fluid in straight pipes by an implicit finite volume method, J. Non-Newt. Fluid Mech. 59 (1995) 191–213.
[12] P. Yue, J. Dooley, J.F. Feng, A general criterion for viscoelastic secondary flow in pipes of noncircular cross section, J. Rheol. 52 (2008) 315–332.
[13] C.G. Speziale, On nonlinear K–l and K–ε models of turbulence, J. Fluid Mech. 178 (1987) 459–475.
[14] H.A. Barnes, J.F. Hutton, K. Walters, An Introduction to Rheology, Elsevier, 1989.
[15] J.G. Oldroyd, On the formulation of rheological equations of state, Proc. Roy. Soc. London A 200 (1950) 523–541.
[16] N. Phan-Thien, R.I. Tanner, A new constitutive equation derived from network theory, J. Non-Newt. Fluid Mech. 2 (1977) 353–365.
[17] R.B. Bird, P.J. Dotson, N.L. Johnson, Polymer solution rheology based on a finitely extensible bead-spring chain model, J. Non-Newt. Fluid Mech. 7 (1980) 213–235.
[18] M.D. Chilcott, J.M. Rallison, Creeping flow of dilute polymer solutions past cylinders and spheres, J. Non-Newt. Fluid Mech. 29 (1988) 381–432.
[19] Y.L. Joo, E.S.G. Shaqfeh, Viscoelastic poiseuille flow through a curved channel – a new elastic instability, Phys. Fluids A 3 (1991) 1691–1694.
[20] Y. Fan, R.I. Tanner, N. Phan-Thien, Fully developed viscous and viscoelastic flows in curved pipes, J. Fluid Mech. 440 (2001) 327–357.
[21] M. Norouzi, M.H. Kayhani, C. Shu, M.R.H. Nobari, Flow of second-order fluid in a curved duct with square cross-section, J. Non-Newt. Fluid Mech. 165 (2010) 323–339.
[22] R.B. Bird, R.C. Armstrong, O. Hassager. Dynamics of Polymeric Liquids. Vol. 1: Fluid Mechanics, Wiley, New York, 1987.
[23] A. Groisman, V. Steinberg, Efficient mixing at low reynolds numbers using polymer additives, Nature 410 (2001) 905–908.
[24] J. Zilz, R.J. Poole, M.A. Alves, D. Bartolo, B. Levache, A. Lindner, Geometric scaling of a purely elastic flow instability in serpentine channels, J. Fluid Mech. 72 (2012) 203–218.
[25] R.J. Poole, M.A. Alves, P.J. Oliveira, Purely elastic flow asymmetries, Phys. Rev. Lett. 99 (2007). 164503.
[26] M.A. Alves, R.J. Poole, Divergent flow in contractions, J. Non-Newt. Fluid Mech. 144 (2007) 140–148.
[27] R. Fattal, R. Kupferman, Constitutive laws of the matrix-logarithm of the conformation tensor, J. Non-Newt. Fluid Mech. 123 (2004) 281–285.
[28] A. Afonso, P.J. Oliveira, F.T. Pinho, M.A. Alves, The log-conformation tensor approach in the finite-volume method framework, J. Non-Newt. Fluid Mech. 157 (1–2) (2009) 55–65.
[29] A. Afonso, P.J. Oliveira, F.T. Pinho, M.A. Alves, Dynamics of high-Deborah number entry flows: a numerical study, J. Fluid Mech. 677 (2011) 272–304.
[30] M.A. Alves, P.J. Oliveira, F.T. Pinho, Benchmark solutions for the flow of Oldroyd-B and PTT fluids in planar contractions, J. Non-Newt. Fluid Mech. 110 (2003) 45–75.
[31] P.J. Oliveira, F.T. Pinho, G.A. Pinto, Numerical simulation of non-linear elastic flows with a general collocated finite-volume method, J. Non-Newt. Fluid Mech. 79 (1998) 1–43.